New Insights into $Mn_{1-x}Zn_xFe_2O_4$ via Fabricating Magnetic Photocatalyst Material $BiVO_4/Mn_{1-x}Zn_xFe_2O_4$

Taiping Xie [1,2], Chenglun Liu [1,3,*], Longjun Xu [1] and Hui Li [3]

[1] State Key Laboratory of Coal Mine Disaster Dynamics and Control, Chongqing University, Chongqing 400044, China; deartaiping@163.com (T.X.); xulj@cqu.edu.cn (L.X.)

[2] Chongqing Key Laboratory of Extraordinary Bond Engineering and Advanced Materials Technology (EBEAM), Yangtze Normal University, Chongqing 408100, China

[3] College of Chemistry and Chemical Engineering, Chongqing University, Chongqing 400044, China; lihui@163.com

[*] Correspondence: xlclj@cqu.edu.cn

Abstract: $BiVO_4/Mn_{1-x}Zn_xFe_2O_4$ was prepared by the impregnation roasting method. XRD (X-ray Diffractometer) tests showed that the prepared $BiVO_4$ is monoclinic crystal, and the introduction of $Mn_{1-x}Zn_xFe_2O_4$ does not change the crystal structure of $BiVO_4$. The introduction of a soft-magnetic material, $Mn_{1-x}Zn_xFe_2O_4$, was beneficial to the composite photocatalyst's separation from the liquid solution using an extra magnet after use. UV-vis spectra analysis indicated that $Mn_{1-x}Zn_xFe_2O_4$ enhanced the absorption intensity of visible light for $BiVO_4$. EIS (electrochemical impedance spectroscopy) investigation revealed that the introduction of $Mn_{1-x}Zn_xFe_2O_4$ enhanced the conductivity of $BiVO_4$, further decreasing its electron transfer impedance. The photocatalytic efficiency of $BiVO_4/Mn_{1-x}Zn_xFe_2O_4$ was higher than that of pure $BiVO_4$. In other words, $Mn_{1-x}Zn_xFe_2O_4$ could enhance the photocatalytic reaction rate.

Keywords: magnetic photocatalyst; electron transfer; reaction kinetics; $BiVO_4$; Mn-Zn ferrite; impregnation roasting method

1. Introduction

Photocatalysis and photocatalytic technology, which uses semiconductor materials to directly absorb and transmute renewable solar light energy into chemical energy, have been considered as promising methods to resolve environmental and energy problems facing the human population [1]. To date, cleaning up organic compounds via degradation and water splitting to produce H_2 are the two most important applications of photocatalysis and its corresponding technology, which are aimed at environmental pollutant treatment and molecular hydrogen production, respectively [2].

In spite of the promising results regarding solar-light-driven photocatalysts, there are still some challenges inhibiting their practical application. The most pressing problem concerns the photocatalytic reaction kinetics using photocatalysts under solar light irradiation [3]. Most of the degradation reactions under solar light irradiation are very slow (they may take several hours). Therefore, it is very important to exploit new and highly efficient photocatalysts. In addition, the intrinsic relationship between photocatalytic activity and photocatalytic material structure can be elucidated by studying the photocatalytic mechanism, which will guide the synthesis and application of new and more efficient photocatalytic systems.

A monoclinic scheelite structure, $BiVO_4$, with a better absorption ability of visible light, has attracted a great deal of attention due to its a relatively narrow band gap. The hybridization of Bi^{6s}-O^{2p}

orbitals upshifted the valence band of monoclinic $BiVO_4$ to a lower potential at about +2.4 eV [2,4–7]. Nonetheless, the photocatalytic efficiency of $BiVO_4$ is generally low because of its poor electron transfer and slow reaction kinetics.

Given that the photocatalyst materials could not be thoroughly recycled from a liquid solution after reaction, secondary pollution would probably be induced by the residual photocatalyst. This prevents it application as a wastewater treatment. Fortunately, a magnetic photocatalyst could solve the above issue [8,9]. The exploitation and application of various magnetic photocatalyst materials have been boosting scientists' morale.

Here, we use $Mn_{1-x}Zn_xFe_2O_4$ as a soft-magnetic substrate to prepare magnetic photocatalyst $BiVO_4/Mn_{1-x}Zn_xFe_2O_4$. In the composite system, the magnetic substrate, $Mn_{1-x}Zn_xFe_2O_4$, facilitated the recovery of the photocatalyst from the liquid reaction solution using an extra magnet after the reaction. Most importantly, $Mn_{1-x}Zn_xFe_2O_4$ could enhance the photocatalytic reaction rate of $BiVO_4$ by enhancing the absorption intensity of visible light for $BiVO_4$ and heightening the conductivity of $BiVO_4$. We sincerely hope to extend the application field of $Mn_{1-x}Zn_xFe_2O_4$ according to this report.

2. Experimental Procedure

All reagents purchased from Sinopharm Chemical Reagent Co., Ltd. (Shanghai, China) were of analytical grade purity and were used directly without further purification. The water used in all experimental processes was deionized water.

2.1. Preparation of $BiVO_4/Mn_{1-x}Zn_xFe_2O_4$

Preparation of $Mn_{1-x}Zn_xFe_2O_4$ [10]. $ZnSO_4$, $MnSO_4$, and $FeCl_3 \cdot 6H_2O$ with a given molar ratio of n (ZnO): n (MnO): n (Fe$_2$O$_3$) = 13.3:32.8:53.9 was separately weighed and dissolved in water to form three solutions. Subsequently, the prepared $ZnSO_4$ solution and $FeCl_3$ solution were added into the $MnSO_4$ solution under continuous stirring condition, in order to form the mixture solution. A definite amount of $(NH_4)_2C_2O_4 \cdot H_2O$ was dissolved to form a $(NH_4)_2C_2O_4$ solution. The prepared mixture solution was slowly added into the $(NH_4)_2C_2O_4$ solution, and the mixture solution and $(NH_4)_2C_2O_4$ solution were heated to 80 °C, respectively. The pH value of the whole reaction system was adjusted to 7 by slowly adding NaOH solution, and a large quantity of precipitate was observed. The precipitate was washed using water and dried at 80 °C for 12 h after filtrating to gain the precursor. The precursor was sintered at 1200 °C for 3 h to form the resultant magnetic substrate, $Mn_xZn_{1-x}Fe_2O_4$.

Preparation of $BiVO_4$ [11]. First, 0.01 mol $Bi(NO_3)_3 \cdot 5H_2O$ and 0.02 mol tartaric acid were dissolved using a certain amount of 2 mol/L HNO_3 solution to form a mixture solution A. Then, its pH value was adjusted to 7.5. Subsequently, 0.01 mol NH_4VO_3 was dissolved in 50 mL hot water (70 °C) to form solution B. Solution A and solution B were mixed to form the precursor of $BiVO_4$. The precursor was dried at 80 °C for 24 h and then sintered at 500 °C for 4 h to obtain pure $BiVO_4$.

Preparation of $BiVO_4/Mn_{1-x}Zn_xFe_2O_4$. First, 0.01 mol $Bi(NO_3)_3 \cdot 5H_2O$ and 0.02 mol tartaric acid were dissolved with a certain amount of 2 mol/L HNO_3 solution to form a mixture solution A. Then, its pH value was adjusted to 7.5. Subsequently, 0.01 mol NH_4VO_3 was dissolved in 50 mL hot water (70 °C) to from solution B. Solution A and solution B were mixed to form C solution. Then, 15.0 wt % $Mn_xZn_{1-x}Fe_2O_4$ was added to solution C. $BiVO_4/Mn_xZn_{1-x}Fe_2O_4$ (15.0 wt %) was obtained after the mixture was dried at 80 °C for 24 h and then sintered at 500 °C for 4 h. The composites $BiVO_4/Mn_xZn_{1-x}Fe_2O_4$ (10.0%, 20.0%, 25.0 wt %) were prepared by adjusting the mass ratio of $Mn_xZn_{1-x}Fe_2O_4$.

2.2. Materials Characterization

The structure characterization of the samples was determined by X-ray Diffractometer (Shimadzu, XRD-6000, Kyoto, Japan), Fourier transform infrared spectroscopy (FTIR, Perkin-Elmersystem 2000, Akron, OH, USA), and INVIA Raman microprobe (Renishaw Instruments, Wotton-under-Edge, UK). The light absorption properties, magnetization, and surface performances of products were

examined by an ultraviolet-visible diffuse reflectance spectrophotometer (UV-vis, DRS, TU1901, Company, Beijing, China), vibrating sample magnetometer (VSM 7410, Lake Shore, Carson, CA, USA), Brunauer−Emmett−Teller (BET, ASAP-2020, Micromeritics, Norcross, GA, USA), and scanning electron microscopy (SEM, EVO-LS15X, ZEISS, Upper Cohen, Germany). The electrochemical workstation (PGSTAT30) was employed to measure the electrochemical impedance spectroscopy (EIS) of samples. The following are the test EIS parameters: $K_3[Fe(CN)_6]$:$K_4[Fe(CN)_6]$ (1:1)-KCl electrolyte solution was employed. The work electrode content contained the prepared photocatalytic materials, acetylene black, and polytetrafluoroethylene (mass ratio, 85:10:5); the counter electrode was platinum foil; and the reference electrode was a saturated calomel electrode (SCE). Finally, the AC (Alternating Current) voltage amplitude was set at 5 mV and the frequency range was 1×10^5~1×10^{-2} Hz.

2.3. Photocatalytic Tests

The photocatalytic activity of the prepared photocatalysts was investigated by the degradation of simulated dye wastewater (Rhodamine B, RhB) under visible light irradiation. One hundred milligrams photocatalyst was put into 100 mL RhB solution with a 5 mg/L concentration, then the suspension liquid was placed in the dark for 0.5 h with stirring to reach the adsorption-desorption equilibrium. A 500 W Xe lamp, equipping with a UV cut-off filter, was used as the visible light source ($\lambda \geq 420$ nm). At the given irradiation time intervals, a series of the reaction solution was withdrawn and the absorbance was measured using the UV-vis spectrophotometer (TU-1901).

3. Results and Discussion

Primary analysis of photodegradation revealed that $BiVO_4/Mn_{1-x}Zn_xFe_2O_4$ (15 wt %) was the most efficient in the RhB degradation process under visible light irradiation.

3.1. Structure and Specific Surface Property

Figure 1 shows the XRD patterns of the as-prepared samples. The characteristic spectra of monoclinic crystal $BiVO_4$ was well indexed with the standard card (JCPDS file 14-0688), corresponding to the characteristic diffraction phases of (110), (011), (121), (040), (200), (002), (211), (150), (132), and (042) [12,13]. The diffraction pattern of $Mn_{1-x}Zn_xFe_2O_4$ was fully matched with the standard card (JCPDS file 74-2400), with the characteristic reflection phases (220), (311), (222), (400), (422), (511), (440), (620), and (622) [10].
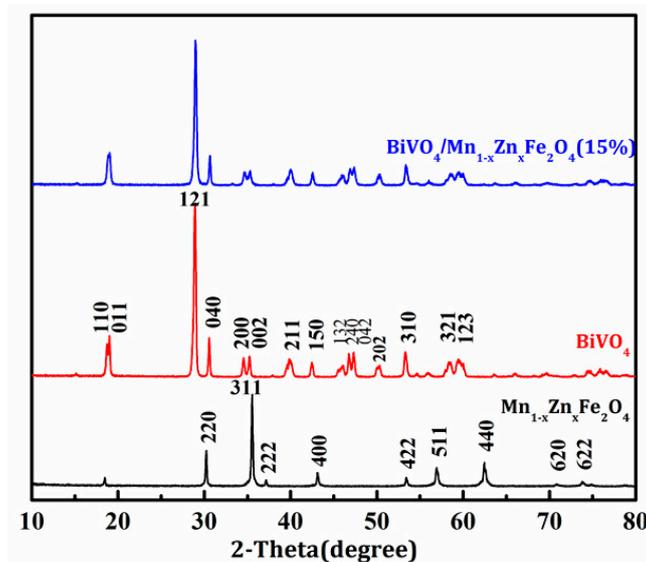

Figure 1. XRD (X-ray Diffractometer) patterns of the prepared samples.

The diffraction peaks of the $Mn_{1-x}Zn_xFe_2O_4$ pattern were difficult to observe in the pattern of $BiVO_4/Mn_{1-x}Zn_xFe_2O_4$ (15 wt %). One the one hand, the intensity of the diffraction peaks of $Mn_{1-x}Zn_xFe_2O_4$ was relatively weak compared with that of the diffraction peaks of $BiVO_4$. On the other hand, the diffraction patterns location of $Mn_{1-x}Zn_xFe_2O_4$ overlapped with the domain diffraction patterns of $BiVO_4$.

The peaks at (121) for $BiVO_4$ in both patterns of pure $BiVO_4$ and $BiVO_4/Mn_{1-x}Zn_xFe_2O_4$ (15 wt %) were clear, even in terms of their intensities. This phenomenon revealed that the introduction of $Mn_{1-x}Zn_xFe_2O_4$ did not alter the growth orientation of $BiVO_4$.

In addition, no impurity phases were found in the $BiVO_4/Mn_{1-x}Zn_xFe_2O_4$ (15 wt %) sample, confirming that there was no appreciable decomposition reaction for $BiVO_4$ and $Mn_{1-x}Zn_xFe_2O_4$ and no perceptible chemical reaction between the two components even though they were sintered at 500 °C.

To further elucidate the structure of $BiVO_4/Mn_{1-x}Zn_xFe_2O_4$ (15 wt %), we carried out the measurement of Fourier transform infrared spectroscopy. Figure 2 illustrates the FTIR spectra of the as-prepared samples. The vibration absorption peaks of Mn-O, Zn-O, and Fe-O bands of $Mn_{1-x}Zn_xFe_2O_4$ were at 560.1 cm^{-1}, 473.7 cm^{-1}, and 412.4 cm^{-1}, respectively [14], while the V-O vibration absorption peaks of $BiVO_4$ were at 734.3 cm^{-1} and 823.4 cm^{-1} [15]. This spectrum of $BiVO_4/Mn_{1-x}Zn_xFe_2O_4$ (15 wt %) could confirm the coexistence of $Mn_{1-x}Zn_xFe_2O_4$ and $BiVO_4$ in the prepared composite, which indicated that $BiVO_4/Mn_{1-x}Zn_xFe_2O_4$ (15 wt %) was prepared successfully. In addition, the absorption patterns at 2341.7 cm^{-1} and 3433.6 cm^{-1} were attributed to CO_2 and the surface adsorption H_2O [9].
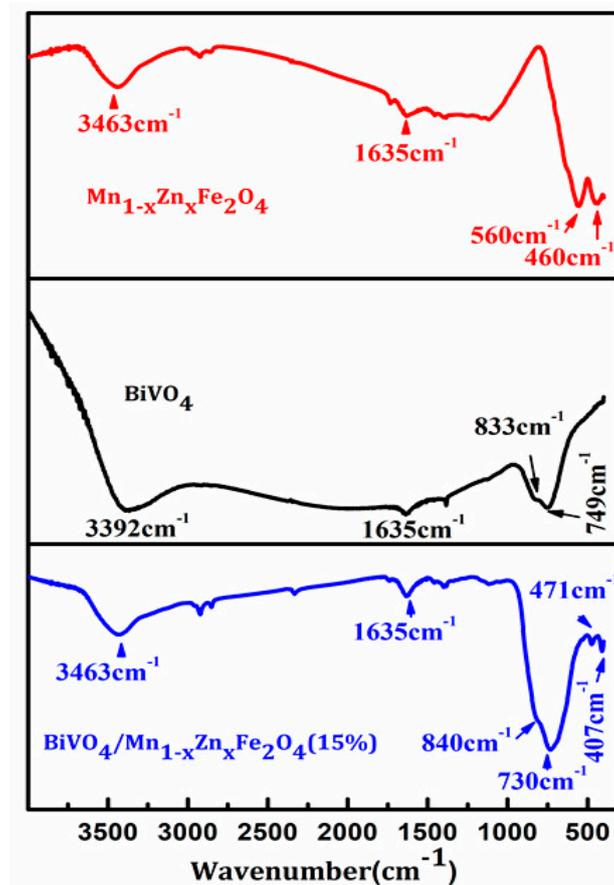

Figure 2. FTIR (Fourier transform infrared) spectrum of the prepared samples.

Raman spectroscopy can provide structural information for materials, and is also a sensitive method to study the crystallization, local structure, and electronic properties of materials. The Raman spectra of the synthesized samples are shown in Figure 3. It can be seen from Figure 3 that the Raman band at 120 cm^{-1}, 210 cm^{-1}, 324 cm^{-1}, 366 cm^{-1}, and 826 cm^{-1} is the typical vibrational band of BiVO$_4$ [16]. These bands could be also observed in the spectroscopy of BiVO$_4$/ Mn$_{1-x}$Zn$_x$Fe$_2$O$_4$ (15 wt %), which further revealed that the BiVO$_4$/Mn$_{1-x}$Zn$_x$Fe$_2$O$_4$ (15 wt %) was synthesized successfully, in agreement with the of XRD and FTIR analysis results. In addition, the intensity of BiVO$_4$ was much larger than that of Mn$_{1-x}$Zn$_x$Fe$_2$O$_4$. So, Mn$_{1-x}$Zn$_x$Fe$_2$O$_4$ signal was not obvious in the spectra of BiVO$_4$/Mn$_{1-x}$Zn$_x$Fe$_2$O$_4$ (15 wt %).
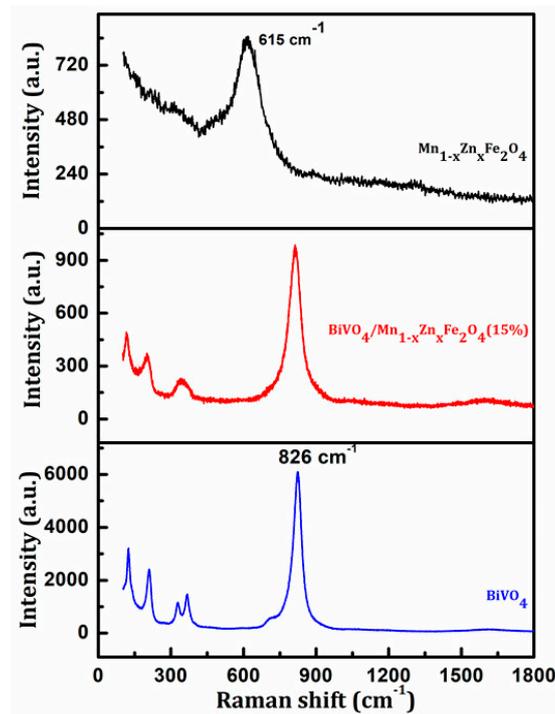

Figure 3. Raman spectra of the prepared samples.

In order to further observe the morphology of the sample, we characterized the material using SEM. Figure 4 is the SEM diagram of the prepared sample: (a) BiVO$_4$, (b) Mn$_{1-x}$Zn$_x$Fe$_2$O$_4$, and (c) BiVO$_4$/Mn$_{1-x}$Zn$_x$Fe$_2$O$_4$ (15 wt %). It can be seen from Figure 4a that pure BiVO$_4$ is a three-dimensional spherical structure, and Figure 4b shows that the prepared Mn$_{1-x}$Zn$_x$Fe$_2$O$_4$ is six-square-like structure. The larger sphere seen in Figure 4c is the core-shell structure of BiVO$_4$ coated with Mn$_{1-x}$Zn$_x$Fe$_2$O$_4$, which indicated that the introduction of Mn$_{1-x}$Zn$_x$Fe$_2$O$_4$ caused the agglomeration of the resultant composite to some extent.

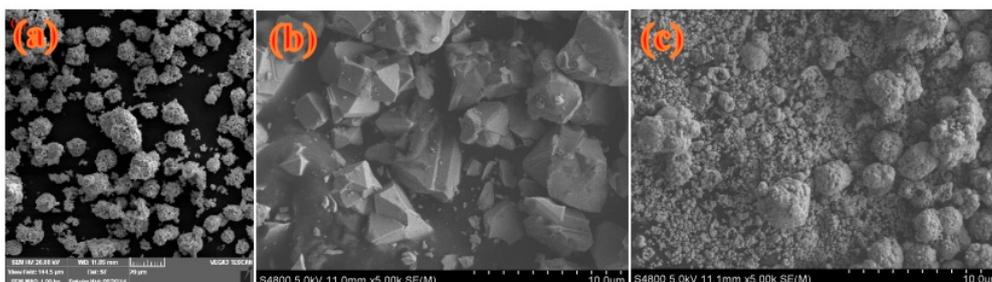**Figure 4.** SEM (scanning electron microscopy) photographs of materials: (**a**) BiVO$_4$, (**b**) Mn$_{1-x}$Zn$_x$Fe$_2$O$_4$, (**c**) BiVO$_4$/Mn$_{1-x}$Zn$_x$Fe$_2$O$_4$ (15 wt %).

Figure 5 shows the N_2 adsorption-desorption isotherm and the pore size distribution curve of $BiVO_4/Mn_{1-x}Zn_xFe_2O_4$ sample. The absorption-desorption isotherm could be categorized as a typical Type III absorption-desorption isotherm [17], indicating that the sample has a porous structure, which was convex to the P/P_0 axis over its entire range, revealing that the as-prepared composite $BiVO_4/Mn_{1-x}Zn_xFe_2O_4$ (15 wt %) belonged to the nonporous structure. This sharp increase in the adsorption isotherm was attributed to the presence of macropores. The most probable pore size of $BiVO_4/Mn_{1-x}Zn_xFe_2O_4$ (15 wt %) is 6.0 nm. In addition, the specific surface area of $BiVO_4/Mn_{1-x}Zn_xFe_2O_4$ sample calculated by BET measurement is 2.22 m^2/g.

vspace-6pt
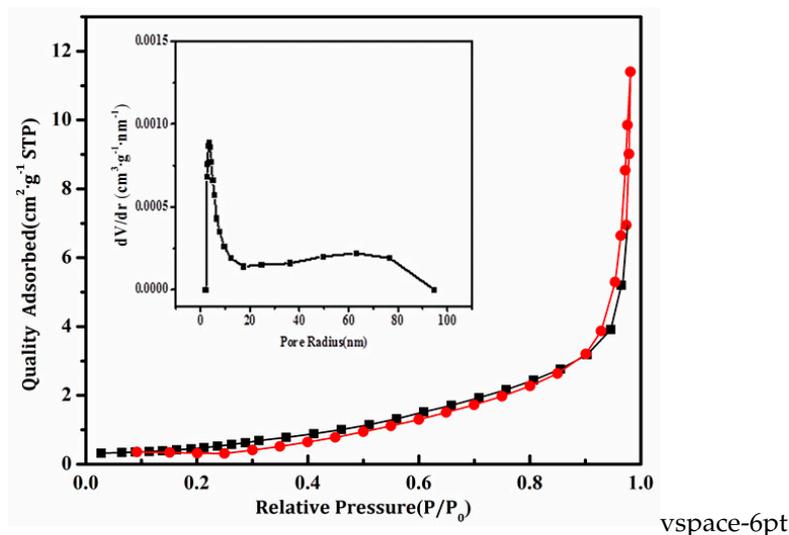
Figure 5. N_2 adsorption-desorption isotherms and pore size distribution curves (insert) of $BiVO_4/Mn_{1-x}Zn_xFe_2O_4$ (15 wt %).

3.2. Magnetic Properties

Figure 6 depicts the hysteresis loops of the magnetic substrate and magnetic photocatalyst $BiVO_4/Mn_{1-x}Zn_xFe_2O_4$ (15 wt %). The saturation magnetization (Ms) and remanent magnetization (Ms) of $BiVO_4/Mn_{1-x}Zn_xFe_2O_4$ (15 wt %) were 84.03 emu/g and 7.03 emu/g, respectively. Compared with pure $Mn_{1-x}Zn_xFe_2O_4$, the Ms of the magnetic photocatalyst decreased by 75.4% and 91.6%, respectively, due to the reduction to the magnetic material content per unit mass of the magnetic photocatalyst [18]. Overall, the magnetic properties of $BiVO_4/Mn_{1-x}Zn_xFe_2O_4$ (15 wt %) were beneficial to its separation from the liquid solution and its recycling from the reaction solution using an extra magnet after use. In addition, the magnetic photocatalyst showed magnetic properties similar to pure $Mn_{1-x}Zn_xFe_2O_4$, which indicated that the magnetic photocatalyst included $Mn_{1-x}Zn_xFe_2O_4$.
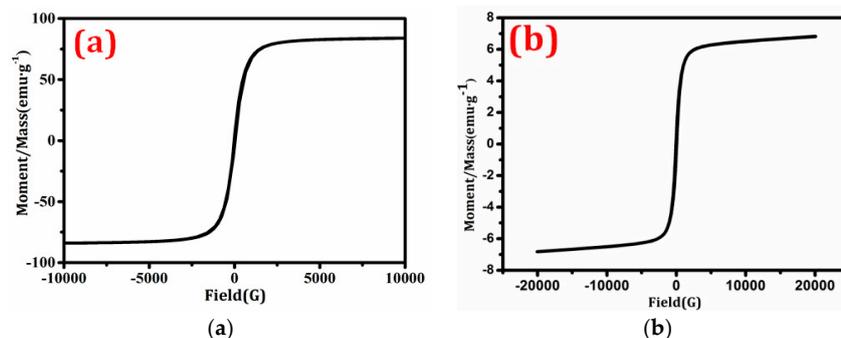

Figure 6. Hysteresis loops of (**a**) $Mn_{1-x}Zn_xFe_2O_4$ and (**b**) $BiVO_4/Mn_{1-x}Zn_xFe_2O_4$ (15 wt %).

3.3. UV-Vis DRS Analysis

The optical absorption properties of semiconductors are considered to be a key factor affecting their photocatalytic activity. Figure 7 shows the UV-Vis diffuse reflectance spectra of $BiVO_4$, $BiVO_4/Mn_{1-x}Zn_xFe_2O_4$, and the curve of $(Ahv)^2$ vs. hv. It can be seen from the diagram that $BiVO_4$ and $BiVO_4/Mn_{1-x}Zn_xFe_2O_4$ mainly absorb light in the wavelength range below 500 nm. Compared with pure $BiVO_4$, the maximum absorption wavelength of $BiVO_4/Mn_{1-x}Zn_xFe_2O_4$ (lambda max) increases, and the absorption of visible light is enhanced to some extent. In addition, the band gap plays a very important role in the determination of photocatalytic activity. The relationship between absorbance and incident light intensity hv can be expressed by the following formula [8,9]:

$$Ahv = C (hv - Eg)^{n/2} \tag{1}$$

In the above equation, A, Eg, h, and v represent the absorption coefficient, band gap width, Planck constant, and incident light frequency, respectively, and C is defined as a constant. The band gap energy of the sample can be obtained from the $(Ahv)^2 \sim hv$ curve. The band gaps (Eg) of $BiVO_4$ and $BiVO_4/Mn_{1-x}Zn_xFe_2O_4$ were estimated. They have nearly the same Eg values (2.36 eV), which are in agreement with the literature [5,19]. Though the incorporation of $Mn_{1-x}Zn_xFe_2O_4$ could not extend the range of absorption light, it is worth noting that the anther function of $Mn_{1-x}Zn_xFe_2O_4$ enhanced the absorption intensity of visible light for $BiVO_4$ by charge transfer transitions ($2Fe^{3+} \rightarrow Fe^{2+} + Fe^{4+}$) [18].
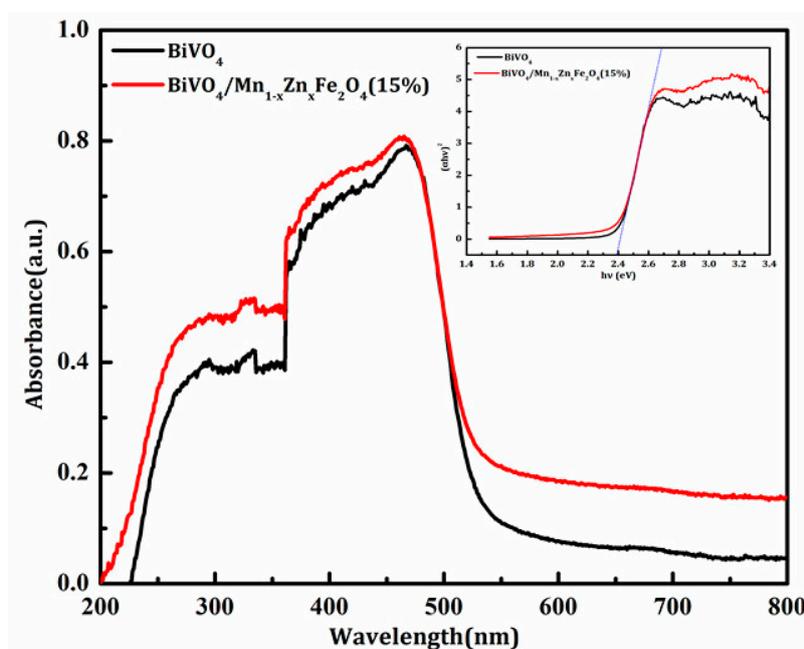
Figure 7. UV-Vis diffuse reflectance spectra of pure $BiVO_4$ and $BiVO_4/Mn_{1-x}Zn_xFe_2O_4$ (15 wt %) samples. Inset: the plot of $(Ahv)^2$ vs. hv to estimate the Eg value.

3.4. Conductivity and Electrochemical Performance

Electrochemical impedance spectroscopy (EIS) is an effective method to evaluate the electron transfer between solid and electrolyte interfaces. Figure 8 shows the Nyquist diagram of the prepared samples. It can be seen from the diagram that the diameter of the semicircle decreases obviously with the introduction of $Mn_{1-x}Zn_xFe_2O_4$, which indicates that the resistance of the solid interface layer and the surface electron transfer impedance decrease. The $BiVO_4/Mn_{1-x}Zn_xFe_2O_4$ charge transfer impedance (206 $\Omega \cdot cm^2$) is less than pure $BiVO_4$ (351 $\Omega \cdot cm^2$) [20]. This is due to the doping effect of Fe ions in the $Mn_{1-x}Zn_xFe_2O_4$ crystal lattice system. The charge transfer was easier, probably due to the charge transfer transitions of Fe ions ($2Fe^{3+} \rightarrow Fe^{2+} + Fe^{4+}$) and Mn ions ($2Mn^{4+} \rightarrow Mn^{2+} + Mn^{6+}$).

The electron transfer impedance of the composite solid /electrolyte interface decreases, which may be because the incorporation of magnetic $Mn_{1-x}Zn_xFe_2O_4$ could enhance the conductivity of $BiVO_4$ and heighten the quantum efficiency of $BiVO_4$. Thus, we can preliminarily predict that the photocatalytic activity of $BiVO_4/Mn_{1-x}Zn_xFe_2O_4$ must be higher than that of pure $BiVO_4$ under the same light irradiation conditions.
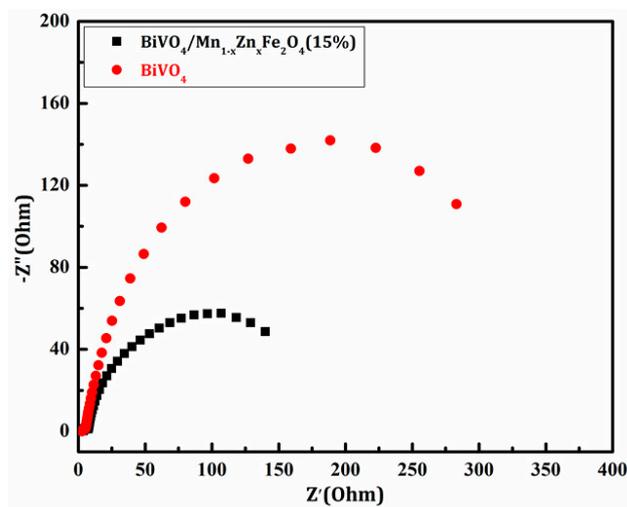

Figure 8. The Nyquist plots of $BiVO_4$ and $BiVO_4/Mn_{1-x}Zn_xFe_2O_4$ (15 wt %).

3.5. Photocatalytic Activity and Stability

The results of the RhB photodegradation by the prepared $BiVO_4$ and $BiVO_4/Mn_{1-x}Zn_xFe_2O_4$ samples are shown in Figure 9. Obviously, the photocatalytic efficiency of $BiVO_4/Mn_{1-x}Zn_xFe_2O_4$ was higher than that of pure $BiVO_4$. Under the same visible light irradiation, the degradation rate of RhB for pure $BiVO_4$ reached 97% after 3 h, while $BiVO_4/Mn_{1-x}Zn_xFe_2O_4$ only took 2 h to achieve the same degradation rate. This result was in good agreement with the EIS analysis. On the one hand, the introduction of $Mn_{1-x}Zn_xFe_2O_4$ enhanced the conductivity of $BiVO_4$, further heightening the electron transfer ability. On the other hand, $Mn_{1-x}Zn_xFe_2O_4$ enhanced the absorption intensity of visible light for $BiVO_4$. Thus, $BiVO_4/Mn_{1-x}Zn_xFe_2O_4$ could produce more photoinduced electron-hole pairs under same visible light irradiation. The two factors generate a synergistic effect to boost the quantum efficiency of $BiVO_4$.
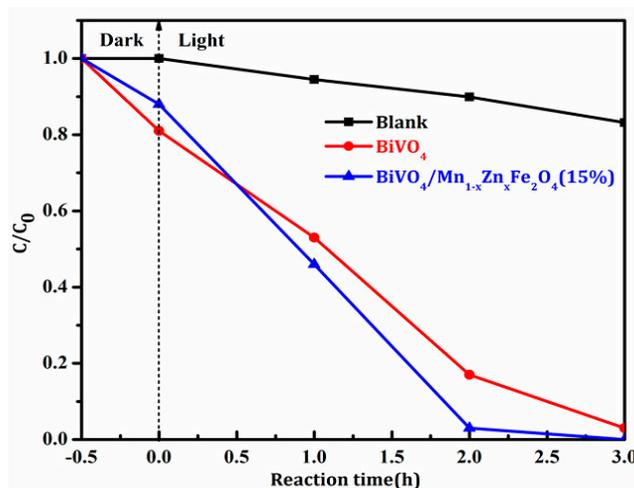

Figure 9. Photocatalytic degradation ratios of RhB with $BiVO_4$ and $BiVO_4/Mn_{1-x}Zn_xFe_2O_4$ (15 wt %) samples.

The repeatability of the magnetic photocatalyst was detected by cycling tests. After each cycle, the catalyst was separated by an external magnet, and then was washed and dried for the next cycle. The degradation rate of RhB using the fifth recycled photocatalyst was still more than 93% (see Figure 10). This indicated that the as-prepared magnetic photocatalyst had an excellent stability. In general, the introduction of a magnetic substrate can enhance the stability of a single component photocatalyst.
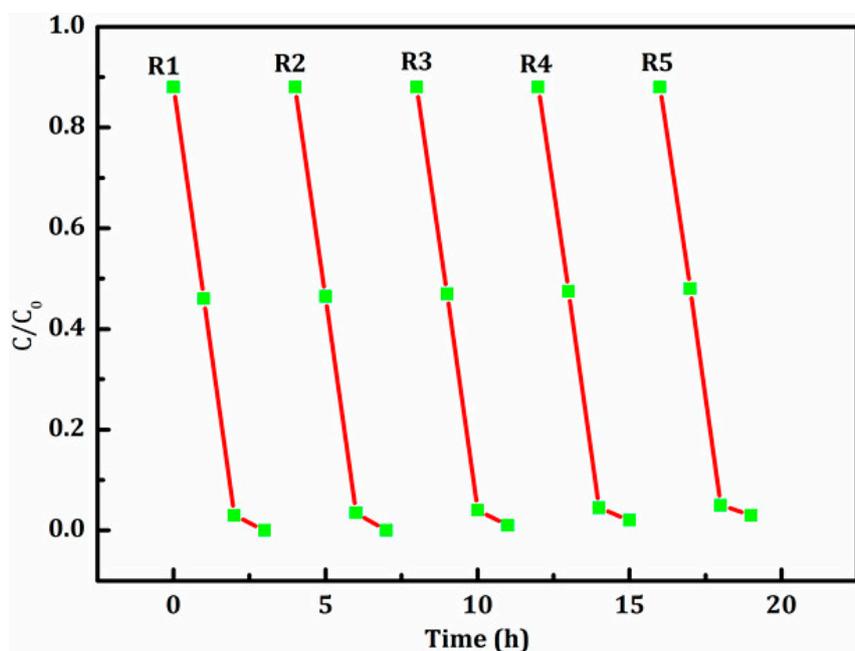

Figure 10. Recycling experiments of degrading RhB with $BiVO_4/Mn_{1-x}Zn_xFe_2O_4$ (15 wt %).

4. Conclusions

$BiVO_4/Mn_{1-x}Zn_xFe_2O_4$ was prepared by the impregnation roasting method. The synthesis method was suitable for the mass production of various composites. XRD tests showed that the prepared $BiVO_4$ is monoclinic crystal, and the introduction of $Mn_{1-x}Zn_xFe_2O_4$ does not change the crystal structure of $BiVO_4$. The introduction of a soft-magnetic material, $Mn_{1-x}Zn_xFe_2O_4$, was beneficial to the composite photocatalyst's separation from the liquid solution using an extra magnet after the reaction. UV-vis spectra analysis indicated that $Mn_{1-x}Zn_xFe_2O_4$ enhanced the absorption intensity of visible light for $BiVO_4$. EIS investigation revealed that the introduction of $Mn_{1-x}Zn_xFe_2O_4$ could decrease the electron transfer impedance of $BiVO_4$, further enhancing its conductivity and heightening its quantum efficiency. The photocatalytic efficiency of $BiVO_4/Mn_{1-x}Zn_xFe_2O_4$ was higher than that of pure $BiVO_4$.

Author Contributions: Taiping Xie and Chenglun Liu conceived and designed the experiments; Taiping Xie and Hui Li performed the experiments; Taiping Xie and Longjun Xu analyzed the data; Chenglun Liu and Longjun Xu contributed reagents/materials/analysis tools; Taiping Xie and Chenglun Liu wrote the paper.

References

1. Nakata, K.; Ochiai, T.; Murakami, T.; Fujishima, A. Photoenergy conversion with TiO_2 photocatalysis: New materials and recent applications. *Electrochim. Acta* **2012**, *84*, 103–111. [CrossRef]

2. Tan, H.L.; Amal, R.; Ng, Y.H. Alternative strategies in improving the photocatalytic and photoelectrochemical activities of visible light-driven $BiVO_4$: A review. *J. Mater. Chem. A* **2017**, *5*, 16498–16521. [CrossRef]

3. Mamba, G.; Mishra, A. Advances in magnetically separable photocatalysts: Smart, recyclable materials for water pollution mitigation. *Catalysts* **2016**, *6*, 79. [CrossRef]

4. Saison, T.; Chemin, N.; Chanéac, C. New insights into $BiVO_4$ properties as visible light photocatalyst. *J. Phys. Chem. C* **2015**, *119*, 12967–12977. [CrossRef]

5. Li, X.; Yu, J.G.; Wageh, S.; Al-Ghamdi, A.A.; Xie, J. Graphene in photocatalysis: A review. *Small* **2016**, *12*, 6640–6696. [CrossRef] [PubMed]

6. Hong, S.J.; Lee, S.; Jang, J.S.; Lee, J.S. Heterojunction $BiVO_4/WO_3$ electrodes for enhanced photoactivity of water oxidation. *Energy Environ. Sci.* **2011**, *4*, 1781–1787. [CrossRef]

7. Sun, J.J.; Li, X.Y.; Zhao, Q.D.; Ke, J.; Zhang, D.K. Novel $V_2O_5/BiVO_4/TiO_2$ nanocomposites with high Visible-light-induced photocatalytic activity for the degradation of toluene. *J. Phys. Chem. C* **2014**, *118*, 10113–10121. [CrossRef]

8. Xie, T.P.; Xu, L.J.; Liu, C.L. Magnetic composite $BiOCl$-$SrFe_{12}O_{19}$: A novel p-n type heterojunction with its enhanced photocatalytic activity. *Dalton Trans.* **2014**, *43*, 2211–2220. [CrossRef] [PubMed]

9. Xie, T.P.; Liu, C.L.; Xu, L.J. Novel heterojunction $Bi_2O_3/SrFe_{12}O_{19}$ magnetic photocatalyst with highly enhanced photocatalytic activity. *J. Phys. Chem. C* **2013**, *117*, 24601–24610. [CrossRef]

10. Zhang, Z.D.; Xu, L.J.; Liu, C.L. Preparation and characterization of composite magnetic photocatalyst $Mn_xZn_{1-x}Fe_2O_4/\beta$-$Bi_2O_3$. *RSC Adv.* **2015**, *5*, 79997–80004. [CrossRef]

11. Liu, C.L.; Li, H.; Ye, H.P.; Xu, L.J. Preparation and visible-light-driven photocatalytic performance of magnetic $SrFe_{12}O_{19}/BiVO_4$. *J. Mater. Eng. Perform.* **2015**, *24*, 771–777.

12. Liu, H.B.; Hou, H.L.; Gao, F.M.; Yao, X.H.; Yang, W.Y. Tailored fabrication of thoroughly mesoporous $BiVO_4$ nanofibers and their visible-light photocatalytic activities. *Appl. Mater. Interfaces* **2016**, *8*, 1929–1936. [CrossRef] [PubMed]

13. Grigioni, I.; Stamplecoskie, K.G.; Selli, E.; Kamat, P.V. Dynamics of photogenerated charge carriers in $WO_3/BiVO_4$ heterojunction photoanodes. *J. Phys. Chem. C* **2015**, *119*, 20792–20800. [CrossRef]

14. Wang, S.H.; Zhou, Q.S. Titania deposited on soft magnetic activated carbon as a magnetically separable photocatalyst with enhanced activity. *Appl. Surf. Sci.* **2016**, *256*, 6191–6198. [CrossRef]

15. Wang, A.L.; Shen, S.; Zhao, Y.B.; Wu, W. Preparation and characterizations of $BiVO_4$/reduced graphene oxide nanocomposites with higher visible light reduction activities. *J. Colloid Interface Sci.* **2015**, *445*, 330–336. [CrossRef] [PubMed]

16. Liu, Z.D.; Lu, Q.F.; Wang, C.Q.; Liu, J.H.; Liu, G.S. Preparation of bamboo-shaped $BiVO_4$ nanofibers by electrospinning method and the enhanced visible-light photocatalytic activity. *J. Alloy. Compd.* **2015**, *651*, 29–33. [CrossRef]

17. Zhou, F.Q.; Fan, J.C.; Xu, Q.J.; Min, Y.L. $BiVO_4$ nanowires decorated with CdS nanoparticles as Z-scheme photocatalyst with enhanced H_2 generation. *Appl. Catal. B* **2017**, *210*, 77–83. [CrossRef]

18. Xie, T.P.; Xu, L.J.; Liu, C.L. Magnetic composite $ZnFe_2O_4/SrFe_{12}O_{19}$: Preparation, characterization, and photocatalytic activity under visible light. *Appl. Surf. Sci.* **2013**, *273*, 684–691. [CrossRef]

19. Singh, S.; Sharma, R.; Mehta, B.R. Enhanced surface area, high Zn interstitial defects and band gap reduction in N-doped ZnO nanosheets coupled with $BiVO_4$ leads to improved photocatalytic performance. *Appl. Surf. Sci.* **2017**, *411*, 321–330. [CrossRef]

20. Chang, X.X.; Wang, T.; Zhang, P. Enhanced surface reaction kinetics and charge separation of p$-$n heterojunction $Co_3O_4/BiVO_4$ photoanodes. *J. Am. Chem. Soc.* **2015**, *137*, 8356–8359. [CrossRef] [PubMed]